Common-path achromatic interferometer-coronagraph: images from a breadboard demonstrator

Alexander V. Tavrov,[1,*] Jun Nishikawa,[1] Motohide Tamura,[1] Lyu Abe,[1] Kaito Yokochi,[2] Takashi Kurokawa,[2] and Mitsuo Takeda[3]

[1]National Astronomical Observatory of Japan, 2-21-1 Osawa, Mitaka Tokyo 181-8588, Japan
[2]Tokyo University of Agriculture and Technology, 2-24-16, Nakamachi, Koganei-shi, Tokyo, Japan
[3]The University of Electro-Communications, 1-5-1, Chofugaoka, Chofu, Tokyo, Japan

*Corresponding author: alxandtv@cc.nao.ac.jp

Received 24 May 2007; revised 27 July 2007; accepted 28 July 2007;
posted 31 July 2007 (Doc. ID 83126); published 21 September 2007

A three-dimensional common-path interferometer is proposed, which can achromatically null out an on-axis source while maintaining the detectability of an off-axis source. A geometric phase in the three-dimensional interferometer introduces an achromatic π-phase shift to the light from the on-axis source, such that destructive interference nulls out the axial light at one of the ports of the interferometer. Light from the off-axis source, which is exempt from destructive interference, comes out from both ports with equal intensity. The common-path scheme makes the system highly immune to environmental disturbances. In the described experiment, a 6×10^{-6} peak-to-peak nulling contrast was obtained.

OCIS codes: 260.3160, 260.5430, 050.5080.

1. Introduction

Achromatic photonic devices are in demand in a variety of optical metrology applications from ultrashort pulse laser beams to radar techniques and astronomical instrumentations [1,2,3]. Planets reflect starlight with apparent brightness of 10^{-7}–10^{-10} of the star emitting light, depending on the wavelength band that extends from infrared to visible. Referring to the Bracewell concept [4], long baseline interferometry enables a high angular resolution technique in which the light from an on-axis bright source interferes destructively, whereas the light from an off-axis low-intensity target interferes constructively such that the off-axis target remains detectable. Many devices for on-axis nulling have recently been proposed, among which are phase [5,6] and pupil masks, delay lines arrays [7], achromatic phase shifters [8], and sophisticated combinations thereof [9]. Among others, a fully achromatic π shifter is a key device that is indispensable for the instrumentation of nulling interferometry and coronagraphy [8].

In an achromatic interferometer-coronagraph (AIC) [10], i.e., a Michelson interferometer with a focusing mirror train in one arm and a plane mirror train in the other arm, both arms have to be adjusted accurately at the zero optical path difference (OPD), which is hard to achieve with a mechanically unstable non-common-path interferometer. In our recent publications [11,12] we proposed a new common-path interferometer scheme that effectively maintains the OPD between the interferometer arms and simultaneously adds an achromatic π-phase shift for destructive interference.

For linearly polarized light, aside from the reflection losses on the mirrors, the interferometer throughput for an on-axis source can attain nearly a 100%–0% power split ratio at the two exit ports of the interferometer, which are referred to as bright and nulled ports. For an off-axis source, equal power comes out from the two ports with a nearly 50%–50% split ratio.

The proposed nulling interferometer requires an arbitrary polarized light to be split in two orthogonal

0003-6935/07/286885-11$15.00/0

linear polarizations, and they can be analyzed by two independent devices. This paper introduces several quantitative experiments that support and complete the previous qualitative studies [11,12].

The paper is organized as follows: after a brief introduction in Section 1, we review the scheme of the proposed three-dimensional nulling interferometer and show its advanced features in Section 2. In Section 3 we describe several nulling experiments with a white light source and an He–Ne laser light. Section 4 contains several notes to achieving a high coronagraphic contrast by the proposed nulling technique. In Section 5 we describe the technical realization of the demonstrator. Prospective developments for the common-path AIC are listed in Section 6.

2. Common-Path Achromatic Interferometer-Coronagraph by Means of Rotational Shearing Interferometer

As shown in Fig. 1, the OPD between two interferometer arms is equal to zero for an on-axis source, denoted by the star mark. Its destructive interference occurs after passing through the achromatic π-phase shifter realized by a rotational shearing interferometer (RSI) [1,13]. An RSI is a differential interferometer with some rotation of the copied wavefront. A similar wavefront folding system with a small amount of rotational shear was extensively studied [14].

An off-axis source, indicated by dots in Fig. 1, introduces a nonzero OPD and produces interference fringes in the pupil plane. In the close vicinity to the axis, the interference remains destructive and has dark fringe localization. Interference becomes no longer destructive, collecting whole light over the pupil plane. A light from such an off-axis source can be detected.

A conventional Sagnac interferometer [15] maintains the OPD because the two interferometer arms are designed to have a common path. For the purpose of nulling, the Sagnac interferometer is extended to three dimensions, as shown schematically in Fig. 2. This interferometer introduces $\pm 90°$ polarization rotations along the forward and the backward light paths. The three-dimensional mirror train consists of six plane mirrors M_1–M_6 and two beam splitters,

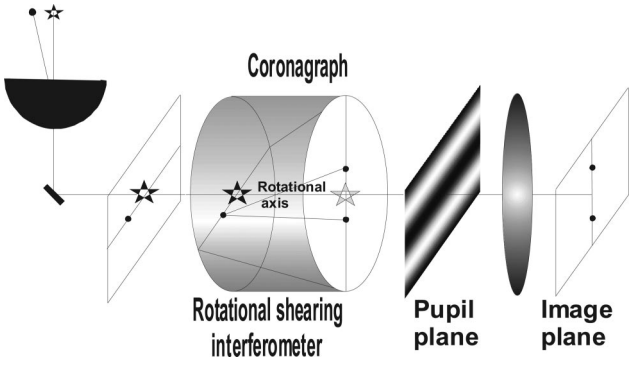

Fig. 1. Basic schematic of nulling for long baseline interferometry and coronagraphy.

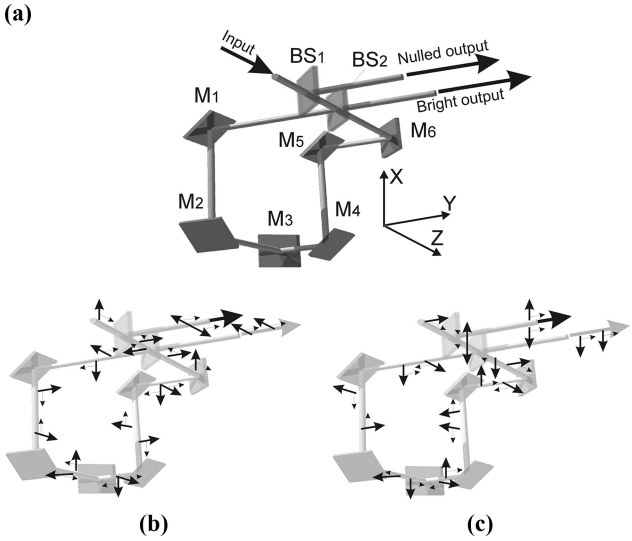

Fig. 2. Common-path interferometer. (a) Schematics, (b), (c) **p** and **s** polarization vector tracing along the interferometer arms.

BS_1 and BS_2. The principal rays are shown along the optical axis in the first interferometer arm, BS_1-BS_2-M_1-M_2-M_3-M_4-M_5-M_6-BS_2-BS_1. The backward path BS_1-BS_2-M_6-M_5-M_4-M_3-M_2-M_1-BS_2-BS_1 introduces the second interferometer arm. The local **p**- and **s**-planes of the mirrors $M_{1–6}$ and the beam splitter BS_2 are oriented out of plane [16] and cause $\pm 90°$ polarization rotations in the first and the second interferometer arms, respectively. With respect to each other, the images in the arms become geometrically rotated by 180°.

Electric vectors follow the image rotation and it introduces an achromatic π-phase shift for destructive interference in the BS_2 port, which faced to the incident beam direction, as shown schematically in Figs. 2(b) and 2(c). The rule of **p**- and **s**-reflections is different, tracing two beams directed from two different output ports of BS_2. The output beam denoted as the Bright output experienced the reflection inside the plate BS, on the optical boundary faced to a lower refraction index medium [17]. The beam redirected back to an incident beam experienced the reflection outside the plate BS, on the boundary faced to a higher refraction index. For a fully symmetrical beam splitter as an ideal cube beam splitter, a $\pi/2$-phase shift occurs at a reflection and two output ports then become π-phase conjugated. Because of the forward and the backward propagations through the same optical path, the proposed design automatically compensates for the chromaticities of the beam splitter and the mirrors, and guarantees the power balance between the two counterpropagating beams, which has been a challenging requirement for the realization of a perfect nulling.

Interference process satisfies the energy conservation law; therefore, in our scheme, one BS_2 port reflects the light that results from the constructive interference and is called as the "bright output" port. The other BS_2 port transmits the rest of the light

energy to the "nulled output" port as the result of destructive interference. The nulled output is reflected to the direction of incident light, and the nulled result is observed via port BS_1. The BS_1 is designed as a broadband polarization beam splitter (PBS). Its transmitting mode is set to match the incident linear polarization state of the input; therefore, almost all energy flux can enter into the interferometer. The interferometer arms rotate the input polarization by $\pm 90°$ so that the polarization of light returning to the BS_1 now matches the reflection mode of the PBS, and again nearly all energy flux can be directed to the nulled port.

The off-axis light component has another interference result: each tilted wave results in two images, and they do not interfere because they are geometrically separated. If the off-axis distance is smaller than the Airy diameter (close-sensing) [2], some fractions of the two images still interfere destructively by overlapping, but the rest of the nonoverlapping images are not nulled out and can be detected.

The present common-path AIC can effectively null the linear polarization with 45° azimuth, because the chromatic properties of the beam splitter BS_2 and the chromatic phase from metal mirrors become all balanced.

The RSI introduces 180°-wavefront rotation, which results in the dependence of nulling performance on the coherence function of the starlight on the pupil plane. For an off-axis component, at each port, the AIC produces two laterally shifted images (symmetric images relative to the optical axis). At their interference, the two point-spread functions (PSFs) superposed with π-phase difference have an imbalance with regard to their amplitudes. The linear phase factor introduced by the wavefront tilt causes the two PSFs to have a lateral shift in an image plane. Therefore the interference contrast at each point is reduced.

In experiment the nulling contrast can be measured directly by the common-path AIC (CPAIC) interferometer. According to the energy conservation law, one beam splitter port emits the bright energy and the other beam splitter nulled port emits the residual energy. A CPAIC directs light from the nulled port and from the bright port to different paths. The corresponding light intensities of the nulled signal I_{Nulled} and the bright signal I_{Bright} can therefore be detected independently, and the nulling contrast is obtained from their ratio,

$$NC = \frac{I_{Nulled}}{I_{Bright}}. \tag{1}$$

If the star is an incoherent circular symmetric disc of radius k_θ in terms of angular spectrum, and the telescope has a uniform clear aperture, then the nulling contrast is given by

$$NC(\Theta) \approx 0.5(1 - (1 - J_0(2k_\theta R))/(k_\theta R)^2), \tag{2}$$

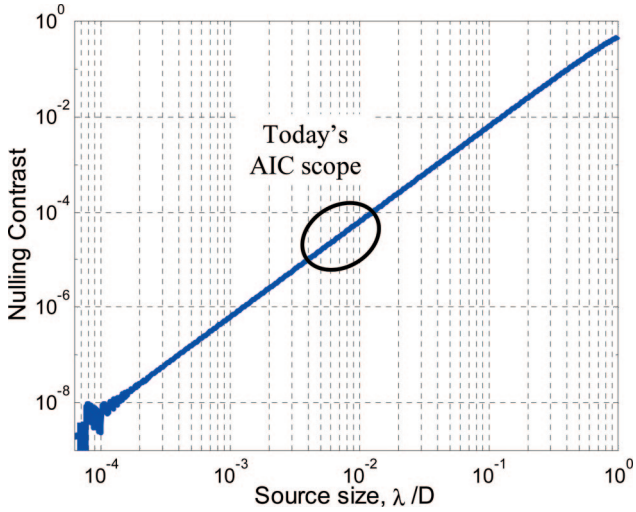

Fig. 3. (Color online) AIC nulling contrast versus the effective source size.

where $2k_\theta R = 2(2\pi/\lambda)(\Theta/2)(D/2) = \pi\Theta D/\lambda$, Θ is the angle diameter of the star, D is the aperture diameter of the telescope, and λ is the wavelength corresponding to the convention of the paper [2].

From its principle, an AIC technique cannot null an extended source, because the extended source is composed of many mutually incoherent off-axis point sources that do not null out. Depending on the effective source size, which is conventionally measured in λ/D units, the nulling contrast (NC) becomes reduced.

The dependence of NC on the source size in unit of (λ/D) calculated from Eq. (2) is graphically shown in Fig. 3. This graph indicates the following nulling contrast for practical source sizes:

$$NC\{0.006(\lambda/D)\} \approx 10^{-5}, \tag{3a}$$

$$NC\{0.002(\lambda/D)\} \approx 10^{-6}. \tag{3b}$$

Equations (3a) and (3b) estimate the practical limitations of the general AIC instrument. Equations (3a) and (3b) correspond to the star with the angular diameters of 1.2 and 0.4 mas, being observed by a 1 m telescope at $\lambda = 1$ μm.

Sophisticated combinations of the AIC technique with other nulling techniques, such as mentioned in [9], can improve these theoretical values. Several factors, such as an extended light source, a polarization mismatch in interference, scattering from optical surfaces, etc., result in a reduced NC. These factors cause the coherence between two interfering beams to degrade, which can be expressed in terms of the complex degree of coherence [18] $\mu(\mathbf{u})$. The real part of μ, denoted by $\mathrm{Re}\{\mu\}$, is a directly measurable quantity, and it is equal to the normalized interference fringe variation in the pupil plane. The vector joining two points brought to the interference in the pupil plane, which are perfectly central symmetrical for an AIC, stands as an argument of μ: $\mu(x, y; -x, -y)$. Then the complex degree of coherence $\bar{\mu}$ averaged

over the pupil is defined as

$$\bar{\mu} = \iint_{\text{Pupil}} A(x, y)[\mu(x, y; -x, -y)]\mathrm{d}x\mathrm{d}y \Big/ \iint_{\text{Pupil}} A(x, y)\mathrm{d}x\mathrm{d}y, \quad (4)$$

where $A(x, y)$ is the intensity transmittance of the aperture so that $\iint_{\text{Pupil}} A(x, y)\mathrm{d}x\mathrm{d}y$ is proportional to the optical power when nulling does not apply. For the proposed CPAIC operating at a single linear polarization, the denominator of Eq. (4) is the power of light collected at this polarization. For unpolarized light it is a nearly half of the total power collected by a telescope. Then the NC averaged over the image plane can be found as

$$\mathrm{NC} \approx (1 - \mathrm{Re}\{\bar{\mu}\})/(1 + \mathrm{Re}\{\bar{\mu}\}). \quad (5)$$

Here we have introduced a new parameter of the averaged complex degree of coherence $\bar{\mu}$ defined by Eq. (4), because it has the advantages that one can obtain both the residual intensity and the nulling contrast solely from the directly measurable quantity, i.e., the coherence function of the light after passing through the imperfect instrumentation of a telescope and a nuller, and also that one need not assume any previous knowledge about the coherence and the irradiance of the light source, which are generally unknown *a priori*. A code for polarization ray tracing was implemented to estimate the tolerances of alignment, polarization settings, ray aberrations, etc., required for the desired NC, and also to predict the reduction of the averaged complex degree of coherence $\bar{\mu}$ taking both source and apparatus into consideration.

To avoid confusion with other papers' terminology for coronagraphy, the term NC will always be used when referring to the coronagraphic performance, while the term "extinction ratio" used later in this paper always refers to beam splitter characteristics.

3. Laboratory Experiments

To confirm the achromatic nulling property by simple experiments with the proposed three-dimensional common-path interferometer and to measure its nulling characteristics, we constructed a breadboard demonstrator, whose optical setup is shown in Fig. 4. Basically, we made use of two separate light sources, which were a halogen lamp and a superluminescent diode (SLD) aligned on-axis and off-axis, respectively. These light sources were combined by the beam splitter BS_0. An SLD emitting the light over a 20 nm spectral width was used to construct the off-axis source. The halogen lamp emitted light with a spectral width over a 300 nm that was used to construct the extended on-axis source, and its measured spectrum is inset in Fig. 4.

To obtain spatially coherent illumination we constructed spatial filters. The SLD light was coupled into a single-mode fiber and emitted by a commercial fiber collimator, and therefore the SLD light can be considered as the spatially coherent point-like source. Light from the halogen lamp was transferred through a pinhole, which was placed in the focus of an achromatic lens. Optionally, for experimental examina-

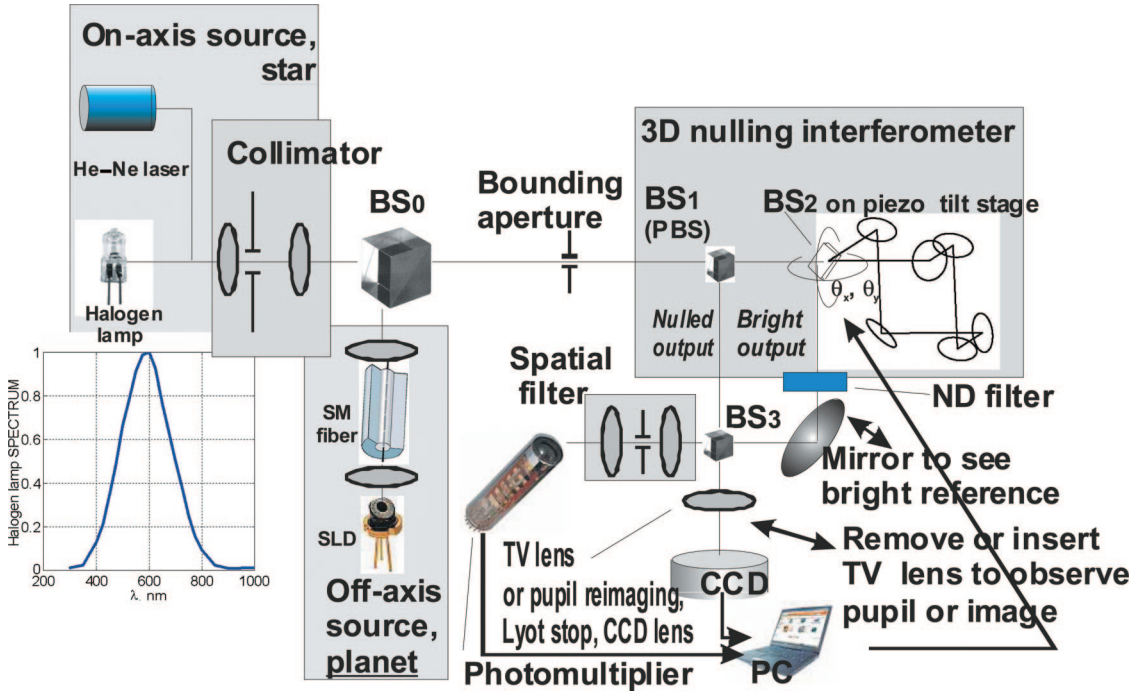

Fig. 4. (Color online) Experimental schematic.

tions, we set various collimation conditions to operate with several effective source angular sizes. To visualize a coherence area with a lensless CCD without a camera lens, the effective source size was set to about 12 arc min (20 μm pinhole in 6 mm focus).

To enable the observation of a reasonable nulling contrast by our breadboard experiment with incoherent white light, we have realized an experimental condition for the theoretical value of NC $\{0.02(\lambda/D)\} \approx 10^{-3}$ with the following collimation setup: a source of the angular size 10 arc sec, constructed by a 5 μm diameter pinhole and a 100 mm achromatic collimation lens, was observed at $\lambda = 0.6$ μm with an aperture of diameter $D = 0.2$ mm.

We used an He–Ne laser for the alignment purpose and to study the extreme of the deepest nulling by a spatially coherent source. In the optical system shown in Fig. 4, a bounding aperture was used to center the beam to the interferometer axis and to set the beam diameter in the nuller. To precisely control the tilt of an interferometer axis we mounted the beam splitter BS_2 on a piezo tilt stage. We used a calibrated neutral density filter (NDF) to attenuate the light intensity in a bright port. With the beam splitter BS_3 and the mirror (denoted as Mirror) we can combine two ports, namely, the bright port and the nulled port. The detection part has two options, either to observe an image by a CCD camera, or to measure an integrated light intensity by a photomultiplier (PM). A spatial filter was optionally inserted in front of the photomultiplier. In front of the CCD we had a standard TV lens, or we can switch it to an optics composed of a Lyot stop and a focusing lens for pupil reimaging. Their specifications are given in Subsections 3.A and 3.B and in Section 5, where we describe the experiment configuration in more detail. To switch among several experimental configurations, we mounted several optical elements on slide holders, which can be optionally inserted in or removed from the optical path. These elements are shown with ↔ marks.

A. Coherence Area Visualization

The AIC was inserted in the pupil space, and we started to observe it with the lensless CCD camera, so that the beam was directed at the CCD without the use of camera lens. For this experiment the Mirror in Fig. 4 was removed from the optical path, and the TV lens was not used.

The halogen lamp and the SLD light sources were aligned on and off-axis, respectively, and were combined by use of beam splitter BS_0. The interference patterns of each light source are clearly identified in the pupil space, as shown in Fig. 5. In Fig. 5(a), the central dark ring-shaped fringe was caused by the on-axis (extended) source. In Fig. 5(b), the fringes with denser spacing were originated from an off-axis source tilted ≈12 arc min. In Fig. 5(c), both the on-axis and the off-axis sources were superimposed, and their fringes localizations showed destructive interference on-axis. The latter picture illustrates the

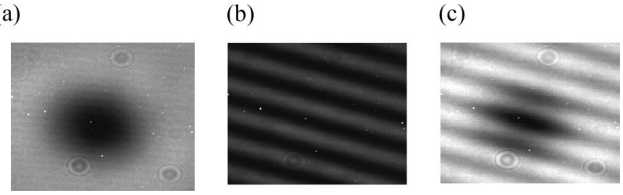

Fig. 5. Pupil plane interference patterns: (a) extended on-axis source, (b) off-axis source, (c) superposition of the on-axis source and the off-axis sources.

principle by which the AIC reduces the on-axis light to detect the off-axis companion light. The fringe localizations are different. The denser fringes are caused by an off-axis source, and we can detect its light on the background of a strong on-axis source, most of which is suppressed by destructive interference. Some residual energy remains not nulled because of the finite size of the on-axis source. In a practical case, the central dark fringe from the on-axis starlight would have a much larger radius, because an observed star size would only be a few milliarcseconds, so the spatial coherence would be greatly increased.

In the experiments shown in Fig. 5, the coherence area was observed with the Airy diameter of 600 μm by the CCD mounted in the plane, which was located at the distance $L \approx 1.5$ m from the collimator lens of diameter $D = 3$ mm and focal length $F = 6$ mm, being focused on the pinhole of diameter $d = 20$ μm; the central wavelength was measured to be $\lambda_0 = 0.55$ μm. The coherence area diameter denoted by $D_{\text{coherence}}$, agrees with the classical diffractometer theory in [19]:

$$D_{\text{coherence}} \approx 3.83\lambda_0 F/(d\pi) + 2L\lambda_0/D, \qquad (6)$$

where the first term corresponds to the coherence area size in the collimator lens plane, and the second term accounts for the λ_0/D diffraction divergence from the finite aperture of the collimator lens. This coherence area corresponds to the giant observed source size of 12 arc min.

B. Achromatic Nulling in Image Plane

To increase the spatial coherence, an effective source size was reduced to nearly 10 arc sec ($0.02\lambda/D$). Under these conditions, the effective diameter of the coherence area of nearly 16 mm was attained and it was larger than the CCD chip size by 1/3 in.; therefore, it cannot be observed with a lensless CCD camera.

To allow the CCD to detect the image plane, we converted the interference patterns from pupil space to image space by attaching a TV lens which focused the light onto a CCD. For demonstration purposes, we used the beam splitter BS_3 to combine two interferometer ports: the nulled and the bright ports within the same CCD frame (Fig. 4). All the optional optical elements mounted on slides, namely the TV lens and the beam splitter Mirror, were now inserted

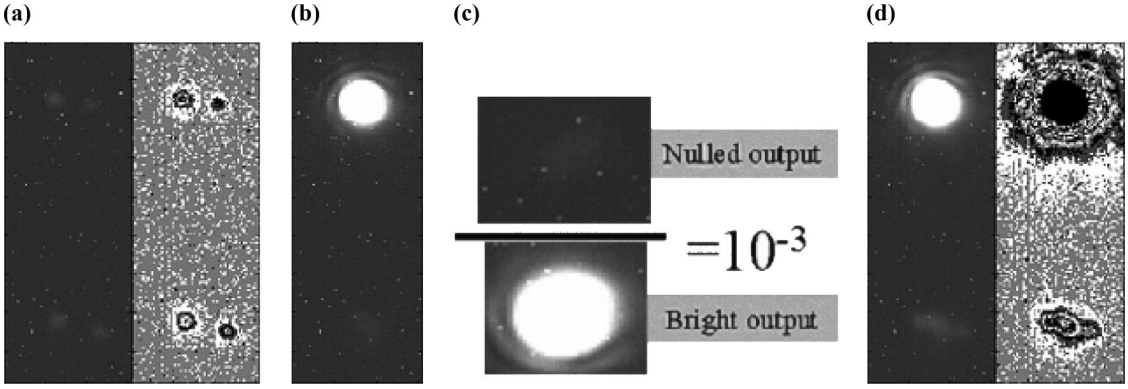

Fig. 6. Achromatic nulling of the on-axis source, the bright output is above the nulled output. (a) Off-axis source switched on; normal display (left) and contrast-enhanced display. (b) On-axis source switched on. (c) Unsaturated intensity values are summed up inside the zoomed areas. The nulling contrast is about 10^{-3}. (d) Both the on-axis and the off-axis sources switched on; normal display (left) and contrast-enhanced display.

in the optical path. We aligned the nulled and bright images one above the other: The upper image area corresponds to the bright output, and the bottom area to the nulled output.

Two interference signals being detected from two sides of the beam combiner satisfy the energy conservation law, so they qualitatively looked complementary: the destructive interference in one signal results in the constructive interference in the other signal.

In Fig. 6(a) the only off-axis source was switched on, and we can observe its image both in the nulled output and in the bright output. The off-axis source is presented as a pair at each output ports, each fraction has the 0.25 of collected energy, and is located symmetrically about an optical axis. We set a low intensity for the off-axis light; shown on the right is a contrast-enhanced image on the CCD thermal noise background. In Fig. 6(b), only the on-axis source is switched on, emitting a relatively strong light intensity. This intensity and the CCD exposure time were optimized to avoid CCD saturation. We can see the strong signal in the upper bright area (shown saturated in the top). In the bottom nulled area, we can still detect some amount of residual energy. To estimate the NC, in Fig. 6(c) we compare the nulled and the bright areas. Their pixel intensities summed up and their ratio showed an NC of $\approx 10^{-3}$, which makes the NC reasonable for a source size of 10 arc sec ($0.02\lambda/D$). In Fig. 6(d), the on-axis and off-axis sources are shown superimposed. Here, in the upper (bright) area, the intensive on-axis component saturates the CCD, and in the nulled area the weak off-axis source can be visually separated. The CCD exposure times for Figs. 6(a)–6(c) were set at 2 min and that for Fig. 6(d) was set at 4 min to demonstrate the mechanical stability of the system.

C. Nulling of He–Ne Laser Light

Experiments aimed to null out a laser source demonstrated a higher contrast because the pupil was illuminated by laser light with sufficiently high spatial coherence. Therefore the interference fringe contrast was not degraded as in the case of white-light source, and the destructive interference can be observed over the whole field of view. Laser radiation has a high degree of spatial coherence, and the laser light emitted from a single spatial mode can be nulled out perfectly, being limited only by the instrument error, which we aim to demonstrate and study.

1. Pupil Plane Image

To compare the light intensities from the nulled output and the bright output we detected them simultaneously in the same CCD frame. Mirror and TV lens were inserted in the optical path. The TV lens was focused on the pupil plane, rather than on the light source, to form two laterally separated images of the pupil on the CCD image sensor, one from the nulled output and the other from the bright output (Fig. 4). A calibrated NDF was inserted in the bright channel to attenuate the bright energy to the level within the CCD dynamical range. Angular alignment of beam splitter BS_1 was performed by two piezo actuators, which aimed to align the interferometer coaxially to the laser. Later on, for the same reason, we used an external piezo-actuated tilt mirror. Then, a partially developed speckle pattern was observed by CCD in the nulled output area (shown in the bottom of Fig. 7), while a more regular pattern was seen in the bright output area, as shown in the top in Fig. 7. Here, the upper spot from the bright port was attenuated by a factor of 2×10^{-4} by use of NDF.

The AIC has the following important property. If a beam incident in the AIC contains some amplitude and wavefront pattern, an ideal AIC would superpose two replicas of this pattern, of which one is rotated 180° around the optical axis, and thereby creates an exit beam that has perfect symmetry with respect to the optical axis of the AIC. These replicas are reflected from the different mirror areas. Considering the local surface figure of the mirror, the optical paths formed by two spatially separated surfaces are not exactly common paths, and they have a small optical path difference introduced by the difference of the local mirror figure. Local vertices of interfering

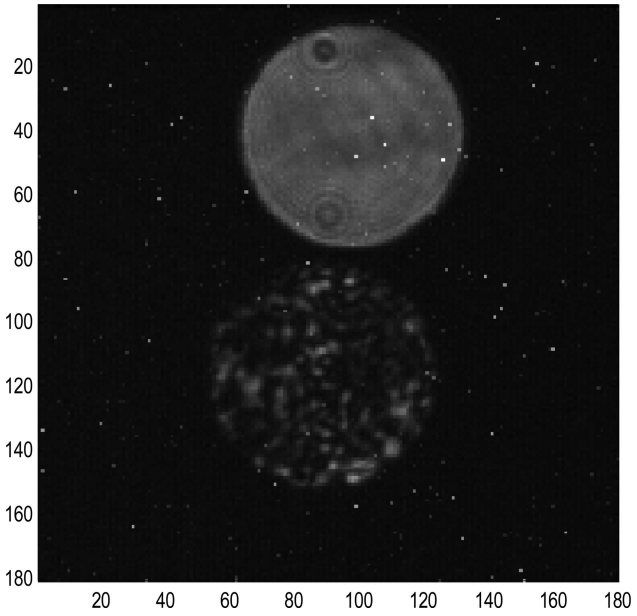

Fig. 7. Partially developed speckles pattern (below). The reference bright image is attenuated in 2×10^{-4} times (above).

beams introduce unequal aberrations caused by different surface figures for counterpropagating wavefronts. Axial-symmetric aberrations are canceled out by an AIC principle.

Following [19], the interference contrast integrated over the pupil will be degraded due to the rms surface roughness of the mirror denoted by δ_0:

$$V \approx \exp\{-(2\pi\delta_0/\lambda)^2\}. \quad (7)$$

If the mirror train consists of statistically independent N mirrors, then the wavefront accumulates the rms error $\delta = \delta_0\sqrt{N}$. Assuming the catalogue peak-to-valley (PV) surface quality, given in fractions of λ (λ/m units), δ_0 for the first surface mirror coated by Al and aligned at 45° beam incidence is well approximated as

$$\delta_0 \approx 2\lambda/(\text{m}5.5 \cos 45°). \quad (8)$$

Just to mention several practical examples, the wavefront quality of $\lambda/1000$ PV is required to obtain the nulling contrast of 10^{-5}: $m \approx 4\pi/(5.5 \cos 45° \sqrt{-\ln(1-10^{-5})}) \approx 10^3$. Stricter requirement for the wavefront at $\lambda/3000$ PV is necessary to attain the nulling of 10^{-6}.

Practically, these are extremely severe requirements, considering that the wavefront is modulated by more than 16 optical surfaces. Forward and backward ray paths result in the doubled number of optical surfaces.

Assuming the peak value of fringe contrast $V \approx 2 \times 10^{-4}$, which was attained experimentally in Fig. 7, we found the mean value of NC $\approx 5 \times 10^{-5}$ averaged over the pupil plane. It corresponds to the wavefront rms error of $\delta \approx \lambda/400$ at $\lambda = 630$ nm. Roughly considering that the contribution from the axially symmetric aberrations is nearly a half of the overall aberrations, a larger wavefront error of $\delta \approx \lambda/300$ can be estimated under the assumption that symmetric aberrations do not influence AIC performance.

As we can see in Fig. 7, the speckle image has many asymmetrical speckle components [20]. Therefore we consider that the observed intensity modulation by speckles does originate from the wavefront modulations inside the AIC. Unwanted modulation is caused by reflections and scattering on M_1–M_6 mirrors, beam splitters (Fig. 2) whose actual surface figures depart from an ideal perfect plane.

Analysis of wavefront accuracy is important to estimate the NC averaged over the pupil. However, it is more suitable for predicting the performance of a CPAIC for a long baseline interferometry (LBLI), rather than for the coronagraph. Coronagraphic image aims to resolve spatial information and to detect a companion at a certain angular position. To understand a speckle pattern in the image plane, and to predict coronagraphic contrast distribution at a certain angular distance in units of λ/D, we need to know the complex amplitude distribution over the pupil with phase information rather than the intensity distribution being detected in the pupil (Fig. 7). It requires accurate wavefront sensing in the pupil plane or, alternatively, just to observe the intensity at the point of interest in the image plane. Therefore in the following experiment we focused on the image plane.

2. Image Plane Pattern

In the image plane we obtained the coronagraphic image at $\lambda = 630$ nm, with the peak-to-peak nulling contrast attained nearly 6.5×10^{-6}, as shown in Fig. 8. Again, two images from the bright port and from the nulled port were aligned with a lateral shift inside the same field of view captured within a single CCD frame. The bright port image was attenuated in 10^{-5} times by the NDF to serve as a reference signal. Bright signal is shown at bottom left in Fig. 8(a). The intensity peak emitted from the nulled port is shown at top right in Fig. 8(a). Figure 8(b) contains only nulled light because the bright port was blocked, and the nulled field of view includes residual speckle noise arising from the imperfection of the nulling apparatus.

Two cross-sectional intensity profiles are shown in Fig. 8(c). The solid curve shows the horizontal intensity profile across the peak of nulled signal. The dashed curve corresponds to the intensity profile evaluated by taking an average in the azimuth direction along the Airy ring, the center of which corresponds to the on-axis position. Figure 8(c) demonstrates the stable nulling contrast of 10^{-6} at $1\ \lambda/D$ distance.

For these measurements we implemented the pupil reimaging technique with a Lyot filter to reduce a diffractional leakage from the edges of bounding ap-

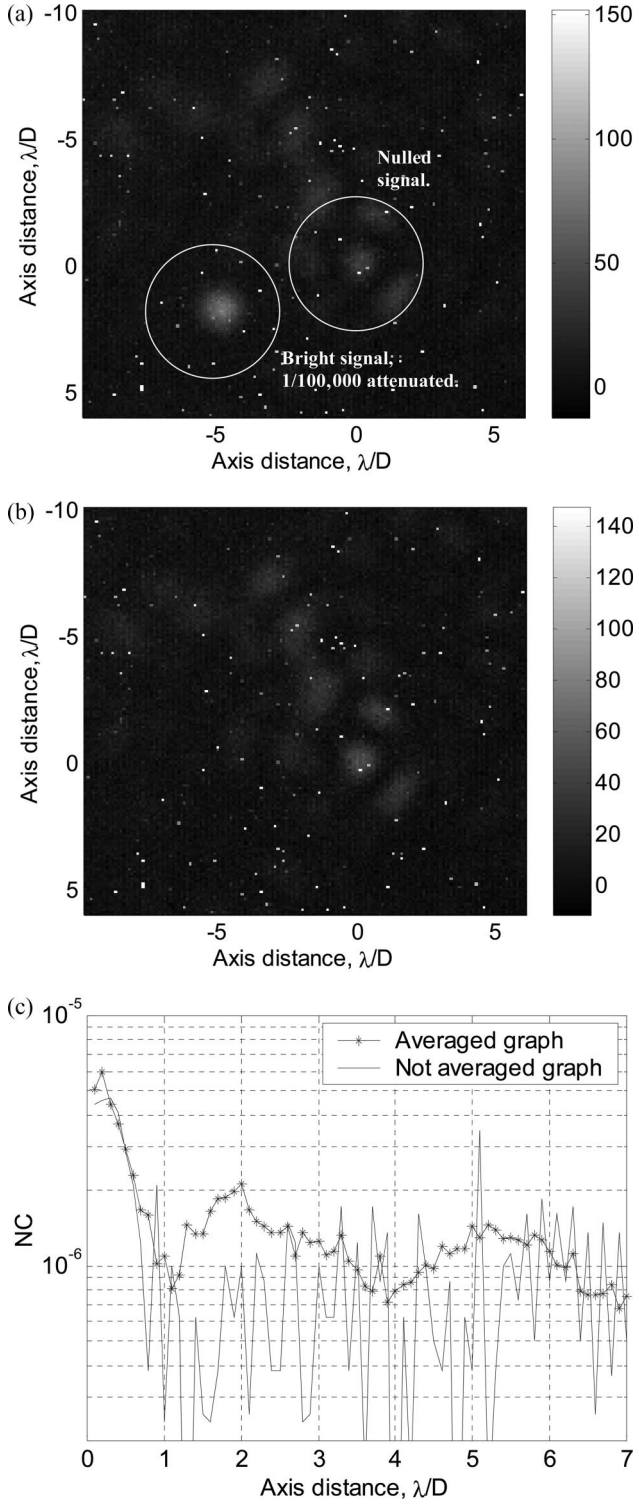

Fig. 8. Peak-to-peak residual speckle contrast around 6.5×10^{-6}. (a) Nulled port image and bright port image for reference is 10^{-5} attenuated (down left). (b) Residual intensity after nulling. (c) Cross-sectional intensity profiles, shown by solid curve, is not averaged, shown by line with * marks, is averaged over the Airy ring with corresponding λ/D radius.

erture. The bounding aperture plane was reimaged by several lenses to the optically conjugated plane to place the Lyot stop in it.

3. *Measurement of Nulling Contrast by the Tilt of Source Axis*

This experiment aimed to measure the angle dependence of nulling capabilities by tracing the null channel signal from the large off-axis un-nulling position to the on-axis nulling position over a true 10^6 dynamical range without taking any reference to the bright channel. It was done by introducing a tilt to the optical axis of the source optics with a pair of precisely controlled piezo actuators. With a (PM) having a sufficiently large dynamic range, we detected NC averaged over the pupil. To improve a wavefront quality, the high spatial frequency components were filtered. The light from the bright port was blocked by keeping Mirror off from the optical path (see Fig. 4). The light emitted from the nulled port was spatially filtered; the beam of $D \approx 2$ mm diameter was focused by an achromatized doublet lens of focal length $F = 80$ mm onto a pinhole of 20 μm diameter. In the pinhole plane, the Airy disk diffraction pattern has the effective diameter of $D_{\text{Airy}} \approx 30$ μm at $\lambda = 0.6$ μm:

$$D_{\text{Airy}} = 1.22\lambda F/D. \tag{9}$$

The pinhole of 20 μm diameter transmitted main optical power and cut off high spatial frequency noise components.

The PM detected the intensity integrated over an image plane. The image shown in the top in Fig. 9 is created from the intensities measured with the PM by means of the synchronized two-dimensional scan of angular position of the source, which was done by introducing tilts (denoted by θ_x, θ_y in Fig. 4) to beam splitter BS_2. BS_2 functions as a device for the angular scan of an interferometer axis by which a fixed source continuously changes in its position from on-axis to off-axis. The angular position of BS_2 was precisely controlled by two piezo actuators and the scan was synchronized with the PM measurements. We also programmed a personal computer (PC) to control two PM amplification parameters, namely, the negative high voltages applied to the PM dynodes and the PM amplifier gain. The necessary calibration of these parameters was stored in a memory to resolve unsaturated light intensities within a 10^6 dynamical range. A lock-in amplifier was used to reduce the influence of an unwanted sidelight.

The image obtained from the scan-synchronized intensity measurement with PM is shown in the top in Fig. 9. Shown in the bottom of Fig. 9 are the cross-sectional intensity profiles of the image along θ_y scan obtained with better resolution. It detects an optical noise from partially developed speckles on the floor of the graph. The cross section shows the minimal intensity values of 9×10^{-6}, which demonstrated the nulling contrast almost down to 10^{-5}.

When the spatial filter was removed from the optical path, we obtained nearly the same nulling contrast with PM as that obtained with the CCD in Fig. 7. We conclude that the best available surface quality

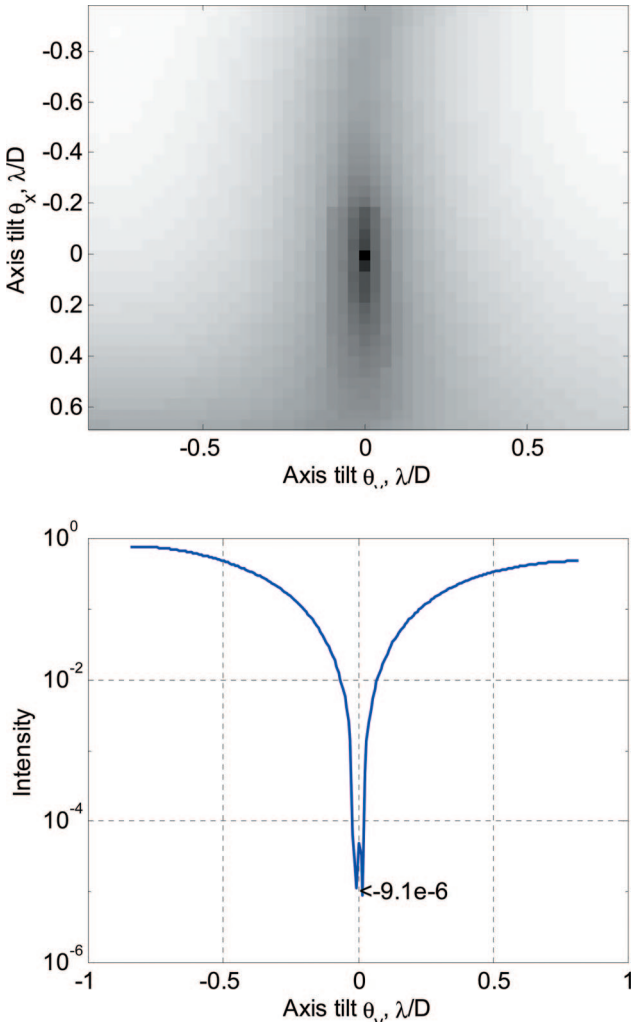

Fig. 9. (Color online) Nulling of spatially filtered image.

mirrors need to be used for the better performance of this common-path AIC, because up to now the mirror roughness is considered as the main limiting factor of the present instrument demonstrator.

4. Several Requirements to Obtain the Peak-to-Peak Nulling Below 10^{-5}

To obtain a peak-to-peak nulling contrast below 10^{-5} experimentally with the described demonstrator, we experienced several technical requirements, which have to be considered for further demonstrator development toward the practical instrument.

A. Mirror Alignment

An actual optical system cannot be aligned perfectly. We computer-modeled (CODEV, MATLAB) the degradation of the nulling contrast, which is caused by the 14 tilts of the misalignment of mirrors $M_{1–6}$ and the beam splitter BS_2. We assumed here the nulling error, which is caused only by improper geometric co-rotations of electrical vectors in a misaligned three-dimensional interferometer, which effects different (nonsymmetric) amounts of polarization rotations by tracing two interferometer arms. We guessed, however, that the beams overlap each other with a perfect coaxial alignment and there is no beam-tilt error and the optics has a perfect quality. We evaluated the nulling contrast versus the maximal angular misalignm error (Table 1), considering first surface Al mirrors at $\lambda = 500$ nm. An accuracy of conventional piezo actuators are enough to obtain the nulling contrast down to 10^{-9}, assuming a coherent point source.

Table 1. Nulling Contrast Versus the Maximal Tilt Misalignment

Maximum misalignment (arc sec)	360	108	36	11	3.6	1.1
Nulling contrast (NC)	10^{-4}	10^{-5}	10^{-6}	10^{-7}	10^{-8}	10^{-9}

B. Polarization Alignment: Polarization Characteristics of Beam Splitters

Polarization characteristics of the beam splitters BS_1 and BS_2 become important to achieve the desired NC via the destructive interference process. In the CPAIC, the same optical element, BS_2, serves as the beam splitter and the beam combiner. The beam splitter BS_2 splits and combines R_sT_p and T_sR_p products, which have to be balanced:

$$R_sT_p = T_sR_p, \tag{10}$$

where R and T denote the reflection and transmission coefficients, respectively, and the subscripts stand for **p**- and **s**-polarization components. This condition in Eq. (10) can be realized by setting the incident linear polarization to have the vibration angle at 45° with respect to the M_1–M_2 rib. Beam splitter BS_2 is chosen to be of dielectric type to prevent an unwanted polarization-dependent phase shift introduced by a metal type beamsplitter.

In the CPAIC demonstrator, the mirrors M_1–M_6 have metal first surfaces, and their **p**- and **s**-reflection coefficients are different and have wavelength dispersion. Therefore in CPAIC, the polarization azimuth rotation mismatches by certain amount of angle δ after $\pm 90°$ image rotations. Polarization azimuth mismatch can be $\delta \approx 15°$ for a metal mirror train and an actual BS_2. However, these δ deviations have a perfectly symmetrical structure; when one arm causes the azimuth rotation equal to $+90° - \delta$, the other arm gives rise to $-90° + \delta$. Therefore polarization azimuths do mismatch by an angle 2δ. The interference contrast can be high enough after two beams pass through the polarizer or the polarizing beam splitter, whose transmission axis is set at bisector, which is 90° to the polarization azimuth on input. The beam splitter BS_1 is a polarizing beam splitter in the CPAIC. A PBS extinction ratio is important to obtain a higher interference contrast and therefore a deeper NC.

It was shown that the peak-to-peak nulling contrast below 10^{-6} can be attained by assuming a 10^3 PBS extinction ratio. The tolerance of the linear polarization azimuth is $45 \pm 0.1°$ on input. The NC

rapidly degrades down to 10^{-4} when the extinction ratio of PBS is lowered to 10^{2}. Both requirements need be fulfilled that polarization azimuth alignment should be within the tolerance of $\pm 0.1°$ and that the extinction ratio should be higher than 10^{3}.

5. Technical Realization

A photograph of the breadboard demonstrator is shown in Fig. 10. Six plane-mirrors were fixed in adjustable holders and were mounted in a solid base to construct three-dimensional mirror train. The mirrors used are first surface mirrors coated by aluminum. We used the plate dielectric beam splitter denoted as BS and the conventional cube polarization beam splitter denoted as PBS in Fig. 10. Ghost light from the plate BS was spatially separated from the principal beam. Ghost light from the rear surface of the cube PBS had the same polarization state as the incident light and it was matched with the PBS transmission mode; therefore, it was mainly transmitted back to the source. A fraction of this ghost light was reflected by PBS to the detector side. We estimate it to be less than 10^{-5} of the light intensity normalized to the incident intensity, assuming the ghost intensity of 1% and the PBS extinction ratio of 10^{3}. A conventional plate PBS does not have an extinction ratio as high as 10^{3}. To improve an extinction ratio we set additional polarizer after the PBS.

A Glan–Taylor PBS offers an excellent extinction ratio of 10^{5} for broadband light, but the specified wavefront figure is usually not better than $\lambda/8$. A Glan–Taylor prism with a good quality could be another candidate to be used as cube PBS.

If we use a plate BS for broadband light we have to consider the lateral pupil shift because of the material dispersion in the plate. This problem becomes critical if we stretch an observation to the smaller beam diameter in a nuller. To maintain the lateral shift caused by a material dispersion, we can use a compensator plate oriented normally to the plate BS. Such a compensator plate has to be manufactured from the same material as the plate BS and has to have the same thickness. In our future work we plan to insert such a compensator plate in the common-path interferometer.

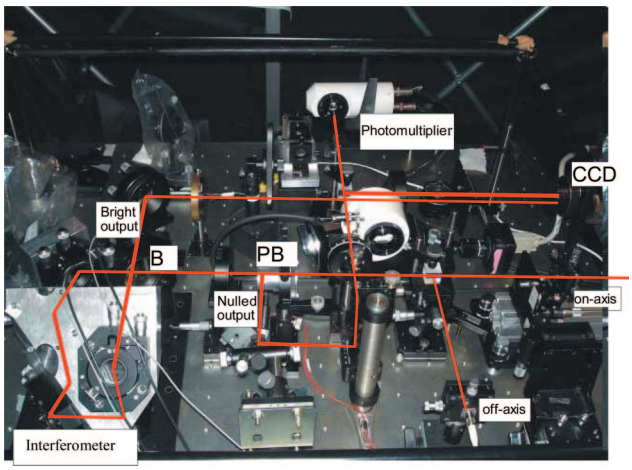

Fig. 10. (Color online) Photo and principal rays in experimental setup.

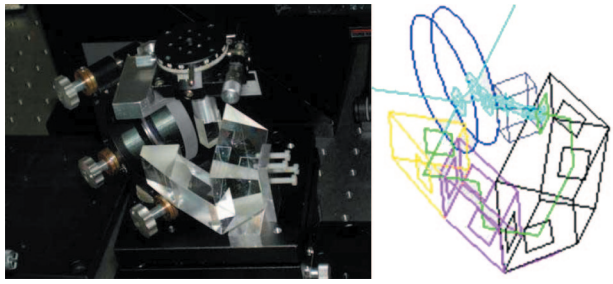

Fig. 11. (Color online) Photo and schematics of prismatic design.

We used pupil reimaging lenses with focal lengths $F = 1000$ mm and $F = 600$ mm (not shown in Fig. 10), a 1 mm diameter Lyot stop, and a focusing CCD lens (TV lens) with $F = 400$ mm. We used commercially available Al-coated first surface mirrors with the nominal peak-to-valley flatness of $\lambda/20$ certified over 30 mm diameter. We reduced the beam size to a 3 mm diameter to operate with better surface figures. It reduced diffractional leakages from optical planes of mirrors and beam splitters, which were not reimaged and not filtered by a single Lyot stop.

We also constructed and examined a prism version of the common-path AIC, which implements the total internal reflections instead of mirror reflections; it was assembled from a custom made glass prism, for which the photograph and the schematic are shown in Fig. 11. The prism version of the common-path AIC is more robust in time, and is more compact and easier in alignment. In the prism version we included a compensator to reduce the chromatic dispersion from plate beam splitter.

6. Perspectives

There are several possible future developments for the described common-path AIC. A future development is to extend the common-path AIC to an infrared (IR) band with the center wavelength of 3–5 μm. With the same optical surface quality of mirrors as we used experimentally in the visible range, we can obtain the nulling contrast at the level 10^{-6}, which is almost the value required for practical implementation by an IR coronagraph. However, a mid-IR wavelength range might require using new materials for transmission optics, and several background issues have to be studied.

Another future challenge is to make use of the extremely wide achromatic properties of the common-path AIC. On-axis source within the wavelength range of 350–2500 nm can be achromatically nulled. Commonly used are advanced differential techniques [21] by spectral differential imaging (SDI) or by image rotation to cancel out the residual light caused by partially developed speckle. To obtain a deep nulling with the CPAIC, a technique can be applied that is

similar to differential imaging to get rid of not-common-path aberration [22].

7. Conclusions

We described the three-dimensional common-path nulling interferometer and tested its characteristics to obtain the deep achromatic nulling contrast aimed for a star coronagraphy. The theoretical and technical predictions showed a reasonable agreement with the computer simulations and the laboratory experiments that demonstrated the achromatic nulling of an on-axis light and the detection of an off-axis light.

A breadboard demonstrator was constructed and we obtained the nulled images from the white-light source of the spectral width over 300 nm in the visible range. We demonstrated experimentally the achromatic nulling depth of approximately 10^{-3}. Taking into consideration extended source properties, the nulling contrast can be improved if we construct a white-light source with smaller effective size, which is technically possible by use of longer collimation length. With laser light we demonstrated the better coronagraphic nulling contrast below 5×10^{-6}. To obtain better nulling contrast at the current stage, we clarified that the main limiting factor is a wavefront quality, because after the reflection and transmission by the optical elements, an entire wavefront became modulated by the surface figures of optics. At the He–Ne laser wavelength we observed partially developed speckles with the interference contrast of 2×10^{-4}, which agreed approximately with the wavefront quality being accumulated by propagation via nuller optics. A perspective on future developments of the common-path AIC technique was presented. The authors hope that the proposed technique, even though presently on the breadboard stage, can become acceptable for practical applications in future.

General AIC principles were originated from the group by Y. Rabbia from the Observatoire de la Côte d'Azur and the authors are grateful to him for helpful suggestions and discussions. We also thank Y. Otani, Y. Takaki, T. Tanaka, and T. Shioda of the Tokyo University of Agriculture and Technology, and M. Pawlowski of the University of Electro-Communications for their technical assistance and helpful suggestions. Part of this work was financially supported by a grant-in-aid (18656018) from the Japan Society for the Promotion of Science, and by the 21st Century Center of Excellence program on "Future Nano-Materials" granted to the Tokyo University of Agriculture and Technology.

References

1. E. Serabyn, J. K. Wallace, G. J. Hardy, E. G. H. Schmidtlin, and H. T. Nguyen, "Deep nulling of visible laser light," Appl. Opt. **38,** 7128–7132 (1999).
2. P. Baudoz, Y. Rabbia, and J. Gay, "Achromatic interfero coronagraphy. I. Theoretical capabilities for ground-based observations," Astron. Astrophys. Suppl. Ser. **141,** 319–329 (2000).
3. N. Baba, N. Murakami, and T. Ishigaki, "Nulling interferometry by use of geometric phase," Opt. Lett. **26,** 1167–1169 (2001).
4. R. N. Bracewell, "Detecting nonsolar planets by spinning infrared interferometer," Nature **274,** 780–781 (1978).
5. D. Rouan, P. Riaud, A. Boccaletti, Y. Clenet, and A. Labeyrie, "The four-quadrant phase mask coronagraph," Publ. Astron. Soc. Pac. **112,** 1479–1486 (2000).
6. F. Roddier and C. Roddier, "Stellar coronograph with phase mask," Publ. Astron. Soc. Pac. **109,** 815–820 (1997).
7. C. van der Avoort, A. Mieremet, S. Pereira, and J. Braat, "Demonstration of nulling using delay line phase shifters," Proc. SPIE **5491,** 816–823 (2004).
8. Y. Rabbia, J. Gay, E. Bascou, and J. L. Schneider, Contract 14398/00/NL/MV Report (European Space Research and Technology Center, 2001).
9. J. Nishikawa, T. Kotani, N. Murakami, N. Baba, Y. Itoh, and M. Tamura, "Combination of nulling interferometer and modified pupil for observations of exoplanets," Astron. Astrophys. **435,** 379–384 (2005).
10. P. Baudoz, Y. Rabbia, J. Gay, R. Burg, L. Petro, P. Bely, B. Fleury, P.–Y. Madec, and F. Charbonnier, "Achromatic interfero coronagraphy II," Astron. Astrophys. Suppl. Ser. **145,** 341–350 (2000).
11. A. V. Tavrov, Y. Tanaka, T. Shioda, T. Kurokawa, and M. Takeda, "Achromatic coronagraph based on out-of-plane common-path nulling interferometer," Proc. SPIE **5491,** 824–830 (2004).
12. A. V. Tavrov, Y. Kobayashi, Y. Tanaka, T. Shioda, Y. Otani, T. Kurokawa, and M. Takeda, "Common-path achromatic interferometer-coronagraph: nulling of polychromatic light," Opt. Lett. **30,** 2224–2226 (2005).
13. M. S. Scholl and G. Paez, "Cancellation of star light generated by a nearby star-planet system upon detection with a rotationally shearing interferometer," Infrared Phys. Technol. **40,** 357–365 (1999).
14. K. Itoh, "Interferometric multispectral imaging," in *Progress in Optics XXXV,* E. Wolf, ed. (Elsevier Science, 1996), pp. 145–196.
15. P. Hariharan, "Interferometers," in *Handbook of Optics 2: Devices, Measurements and Properties,* M. Bass, ed. (McGraw-Hill, 1995), Chap. 21.
16. A. Tavrov, Y. Miyamoto, T. Kawabata, M. Takeda, and V. Andreev, "Generalized algorithm for the unified analysis and simultaneous evaluation of geometrical spin-redirection phase and Pancharatnam phase in a complex interferometric system," J. Opt. Soc. Am A **17,** 154–161 (2000).
17. E. Hecht, *Optics,* 2nd ed. (Addison Wesley, 1995), Chap. 4.3.1.
18. M. Born and E. Wolf, *Principles of Optics,* 7th ed. (Cambridge U. Press, 2002), Chap. 10.
19. W. Traub, "Beam combination and fringe measurement," in *Principles of Long Baseline Stellar Inteferometry,* P. Lawson, ed. (Jet Propulsion Laboratory, 1999), Publ. 00009 07/00, Chap. 3.
20. A. Boccaletti, P. Riaud, and D. Rouan, "Speckle symmetry with high-contrast coronagraphs," Publ. Astron. Soc. Pac. **114,** 132–136 (2002).
21. C. Marois, R. Doyon, R. Racine, D. Nadeau, D. Lafreniere, P. Vallee, M. Riopel, and B. Macintosh, "Direct exoplanet imaging around Sun-like stars: beating the speckle noise with innovative imaging technique," J. R. Astron. Soc. Canada **99,** 130–135 (2005).
22. B. Biller, L. Close, R. Lenzen, W. Brandner, D. McCarthy, E. Nielsen, and M. Hartung, "Supressing speckle noise for simultaneous differential extrasolar planet imaging (SDI) at the VLT and MMT," Proc. SPIE **5490,** 389–397 (2004).